Dynamic regulation of *AtDAO1* and *GH3* modulates auxin homeostasis

Nathan Mellor[a,b], **Leah R Band**[a,b], **Aleš Pěnčík**[c], **Ondřej Novák**[c], **Afaf Rashed**[a], **Tara Holman**[a], **Michael Wilson**[a,d], **Ute Voß**[a], **Anthony Bishopp**[a], **John R King**[a,b], **Karin Ljung**[c], **Malcolm J Bennett**[a,b,1], **and Markus R Owen**[a,b,1]

[a]Centre for Plant Integrative Biology, Division of Plant and Crop Sciences, School of Biosciences, University of Nottingham, Sutton Bonington Campus, Loughborough, LE12 5RD, UK; [b]Centre for Mathematical Medicine and Biology, School of Mathematical Sciences, University of Nottingham, University Park, Nottingham, NG7 2RD, UK; [c]Umeå Plant Science Centre, Department of Forest Genetics and Plant Physiology, Swedish University of Agricultural Sciences, SE-901 83 Umeå, Sweden; [d]Centre for Plant Sciences, School of Biology, Faculty of Biological Sciences, University of Leeds, Leeds LS2 9JT, UK

This manuscript was compiled on July 23, 2016

The hormone auxin is a key regulator of plant growth and development, and great progress has been made understanding auxin transport and signaling. Here we show that auxin metabolism and homeostasis are also regulated in a complex manner. The principal auxin degradation pathways in *Arabidopsis* include oxidation by AtDAO1/2 and conjugation by GH3s. Metabolic profiling of *dao1-1* root tissues revealed a 50% decrease in the oxidation product oxIAA, an increase in the conjugated forms IAA-Asp and IAA-Glu of 438-fold and 240-fold respectively, while auxin remains close to wild type. By fitting parameter values to a mathematical model of these metabolic pathways we show that, in addition to reduced oxidation, both auxin biosynthesis and conjugation are increased in *dao1-1*. We then quantified gene expression *in plantae*, and found that transcripts of *AtDAO1* and *GH3* genes are increased in response to auxin, over different time scales and concentration ranges. Including this regulation of *AtDAO1* and *GH3* in an extended model reveals that auxin oxidation is more important for auxin homoeostasis at lower hormone concentrations, while auxin conjugation is most significant at high auxin levels. Finally, embedding our homeostasis model in a multicellular simulation to assess the spatial effect of the *dao1-1* mutant shows that auxin increases in outer root tissues, in agreement with the *dao1-1* mutant root hair phenotype. We conclude that auxin homeostasis is dependent on *AtDAO1*, acting in concert with *GH3*, to maintain auxin at optimal levels for plant growth and development.

hormone regulation | auxin | metabolism | homeostasis | *Arabidopsis thaliana*

DRAFT

The plant hormone auxin regulates a myriad of processes in plant growth and development [1]. Whilst significant progress has been made in understanding the molecular basis of auxin transport, perception and response, the control of auxin metabolism and homeostasis, via conjugation and degradation, remains less well studied.

Several forms of auxin conjugates have been identified in plants including ester-linked IAA-sugar conjugates and amide-linked IAA-amino acid conjugates [2]. In *Arabidopsis thaliana*, the Gretchen Hagen3 (GH3) family of auxin inducible acyl amido synthetases have been shown to convert IAA to IAA-amino acids [3]. Most amino acid IAA conjugates are believed to be inactive and some, such as IAA-Asp and IAA-Glu, can also be further metabolized [4–6]. The conversion of IAA to IAA-glucose (IAA-Glc) is catalysed by the UDP glucosyltransferase UGT84B1 [7]. The oxidized form of IAA, 2-oxindole-3-acetic acid (oxIAA), has been identified as a major IAA catabolite in *Arabidopsis* [4, 6, 8], and can be further metabolized by conjugation to glucose [9]. OxIAA has been shown to be an irreversible IAA catabolite that has very little biological activity compared to IAA, and is not transported via the polar auxin transport system [6, 8]. Although these metabolites and pathways have been identified, it has been difficult to identify the genes and enzymes involved. Two closely related components of the IAA degradation machinery have recently been identified in Arabidopsis, *DIOXYGENASE FOR AUXIN OXIDATION 1* (*AtDAO1*, *At1g14130*) and *AtDAO2* (*At1g14120*) [10–12]. *AtDAO1* and *AtDAO2* are closely related to genes described in apple (*Adventitious Rooting Related Oxygenase 1*, *ARRO-1* [13]) and rice (*Dioxygenase for Auxin Oxidation*, *DAO* [14]) and a family of GA2 oxidases that mediate degradation of gibberellins (GAs [15]). Radiolabelled IAA feeding studies of loss and gain-of-function *AtDAO1* lines have demonstrated that this oxidase represents the major regulator of auxin degradation to oxIAA in Arabidopsis [11]. Metabolite profiling of mutant lines revealed that disrupting *AtDAO1* regulation resulted in major changes in steady state levels of oxIAA and IAA conjugates, but not IAA. Hence, IAA conjugation and catabolism appear to regulate auxin levels in *Arabidopsis* in a highly redundant manner.

In this paper we describe a systems biology approach to understanding the highly non-linear regulation of auxin homeostasis in *Arabidopsis*. We initially use a mathematical model of auxin metabolism to reveal the importance in *dao1-1* mu-

Significance Statement

Auxin is a key hormone regulating plant growth and development. We combine experiments and mathematical modeling to reveal how auxin levels are maintained within normal physiological limits via feedback regulation of genes encoding key metabolic enzymes. In particular, we describe how regulation of auxin oxidation, via transcriptional control of *AtDAO1* expression, is important at low to normal auxin concentrations. In contrast, higher auxin levels lead to increased *GH3* expression and auxin conjugation, thereby reducing hormone concentration. Integrating this understanding into a multicellular model of root auxin dynamics successfully predicts that the *dao1-1* mutant has an auxin-dependent longer root hair phenotype. Our findings reveal the importance of auxin homeostasis to maintain this hormone at optimal levels for plant growth and development.

N.M., J.R.K., K.L., M.J.B. and M.R.O. designed research; N.M., L.R.B., A.P., O.N., A.R. and M.R.O. performed research; N.M., L.R.B., M.J.B. and M.R.O. analyzed data; and N.M., L.R.B., J.R.K., M.J.B. and M.R.O. wrote the paper.

The authors declare no conflict of interest.

---

[1] To whom correspondence should be addressed. E-mail: markus.owennottingham.ac.uk, malcolm.bennettnottingham.ac.uk

tant plants of not only a reduction in IAA oxidation rate, but a more than 200-fold increase in the rate of irreversible GH3 conjugation coupled with an increase in the rate of IAA biosynthesis. Our transcriptomic data shows that there are feedbacks on the auxin degradation pathway, namely the IAA induction of *AtDAO1* and members of the *GH3* family. To investigate the effect of these feedbacks on auxin homeostasis we add them to an extended model, revealing that the AtDAO1 degradation pathway is much more effective when IAA is at physiological levels, while the GH3 degradation pathway is dominant after high levels of IAA input. Finally, we embed our homeostasis model in a multicellular context that predicts one spatial effect of the *dao1-1* mutant is to increase IAA in outer root tissues, consistent with the auxin-dependent elongated root hair phenotype described for the *dao1-1* mutant [11].

Results

A mathematical model of auxin metabolism predicts the *dao1-1* mutant has altered rates of auxin oxidation, conjugation and synthesis. The principal degradation pathways in Arabidopsis include irreversible conjugation by GH3s and oxidation by AtDAO1/2 (Fig. 1A). In the roots of *dao1-1* knockout seedlings, oxidised IAA (oxIAA) levels are halved and the conjugated forms IAA-Asp and IAA-Glu are increased by 438 and 240-fold respectively, whereas the level of IAA is only increased by 20% (statistically insignificant) (Fig. 1B). These root data are consistent with metabolite profiling from whole seedlings and different tissues [11].

To investigate whether the conceptual model of the main IAA degradation pathways summarised in Fig. 1A is consistent with the metabolite data given in Fig. 1B a linear ordinary differential equation (ODE) model was formulated (see **Materials and Methods**, *SI Appendix*). The model simulates the biosynthesis of IAA and its subsequent conversion to IAA-glc via UGT, to IAA-Asp and IAA-Glu via GH3, and to oxIAA via AtDAO1/2. IAA-glc and oxIAA can both be conjugated further to form oxIAA-glc, and this, along with the conjugates IAA-Asp and IAA-Glu, are then degraded at fixed rates. We calculated steady state levels of the model variables in the wild type, modeled the mutant by setting the rate of AtDAO1-mediated IAA-oxidation in *dao1-1* to zero ($d_1^* = 0$, where the * notation indicates a parameter value in the *dao1-1* mutant), and estimated model parameters to best fit the data in Fig. 1B. The model is able to reproduce the observed reductions in [*oxIAA*] and [*oxIAA-glc*], whilst maintaining levels of [*IAA*] and [*IAA-glc*], but yields only an 8% increase in the levels of conjugated auxin ([*IAA-Asp*]/[*IAA-Glu*]), far less than the experimentally observed changes of greater than 200-fold (Fig. 1C). Thus our mathematical modeling predicts that a decrease in oxidation rate alone is not sufficient to account for the massive increase in conjugation products and IAA homeostasis in *dao1-1*.

To explore whether increased GH3 conjugation rates in *dao1-1* can explain the data, we increased those rates 10-fold in our model so that $g_a^* = 10g_a$ and $g_g^* = 10g_g$. Along with the knock out of *AtDAO1*, this surprisingly results in only a 13% increase in the level of [*IAA-Asp*] and [*IAA-Glu*] conjugates and decreases in all other metabolites (Fig. 1D). We conclude that altering GH3 conjugation rates is insufficient in isolation to explain the metabolic data. We therefore tested in our model whether increasing the auxin biosynthesis rate

DRA

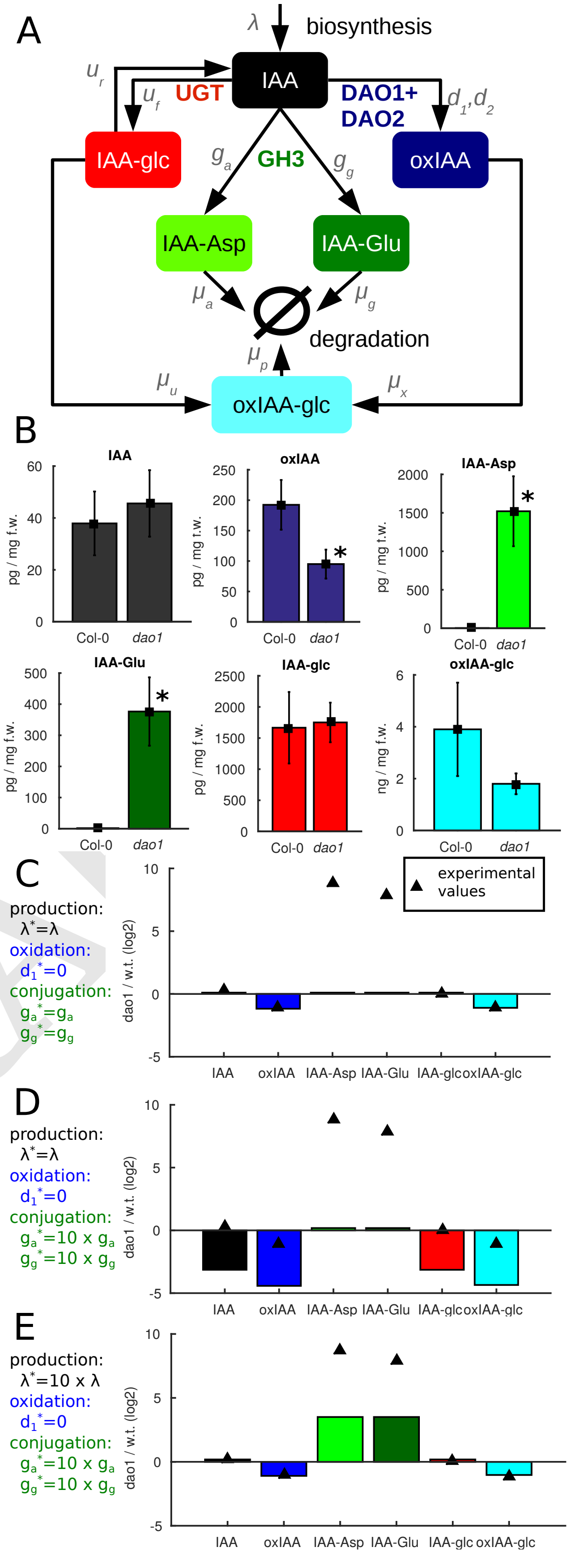

Fig. 1. A metabolic model suggests the *dao1-1* mutant may have altered rates of metabolism other than IAA oxidation. (**A**) The principal degradation pathways in *Arabidopsis* include irreversible conjugation by GH3s and oxidation by DAO1/2. (**B**) In the *dao1-1* knockout, oxidised IAA (oxIAA) levels are halved and conjugated forms, IAA-Asp and IAA-Glu are increased by more than 438 and 240-fold respectively, while the level of IAA is increased by only 20%. Asterisks indicate statistically significant differences from Col-0 (P<0.05, Student's t-test). (**C,D**) Mathematical modeling predicts that a decrease in oxidation rate alone is not sufficient to account for the increase in conjugation products and IAA homeostasis in *dao1-1*, and increasing GH3 conjugation rates does not lead to a better qualitative match. (**E**) Increasing *both* IAA biosynthesis and GH3 conjugation rates in the *dao1-1* simulation can qualitatively match metabolomic data.

in *dao1-1* ($\lambda^* = 10\lambda$) as well as GH3-mediated conjugation rates could capture the experimentally observed behaviour of the *dao1-1* mutant compared to wild type. Fig. 1E shows that increasing *both* IAA biosynthesis and GH3 conjugation rates in the *dao1-1* simulation can qualitatively match metabolomic data. Hence, auxin homeostasis appears to be maintained in the IAA oxidase mutant *dao1-1* by adjusting conjugation and synthesis rates.

Systems analysis reveals that in addition to reduced oxidation, both IAA biosynthesis and conjugation are increased in *dao1-1*. Next we sought experimental evidence for changes in conjugation and synthesis rates, before attempting more precise fitting of our model to the data. Quantitative RT-PCR shows that the mRNA expression level of *GH3.3* is 2.7 times higher in *dao1-1* than in wild type (Fig. 2A), and additional metabolite profiling in whole seedlings shows the levels of the three IAA precursors IAM, IPyA and IAN all drop significantly in the *dao1-1* mutant relative to wild type (Fig. 2B), indicating a higher IAA biosynthetic rate in *dao1-1*.

To further establish the plausibility of increased IAA biosynthesis and GH3 conjugation in the *dao1-1* mutant, model parameters were fitted to the steady state metabolite data for $[IAA]$, $[oxIAA]$, $[IAA\text{-}Asp]$, $[IAA\text{-}Glu]$, $[IAA\text{-}glc]$ and $[oxIAA\text{-}glc]$ in both wild type and *dao1-1*. To fix the IAA synthesis rate in *dao1-1* (λ^*), we assume that IAM, IPyA and IAN have constant production rates (which do not vary between w.t. and *dao1-1*), and that each is converted to IAA at a rate that is different in *dao1-1* compared to w.t.. It follows that λ^* is inversely proportional to the corresponding drop in auxin precursor concentrations (0.74 averaged across IAM, IPyA and IAN), giving $\lambda^* = 1.36$. We then allowed the remaining parameters, including g_a, g_a^* and g_g, g_g^* (the respective rates, in w.t. and *dao1-1*, of GH3 mediated conjugation to $[IAA\text{-}Asp]$ and $[IAA\text{-}Glu]$), to take any values within a wide range of fixed bounds. The parameter fitting used a hybrid genetic algorithm plus local minimum search which sought to minimise the squared difference between model steady state and metabolite data, for both w.t. and *dao1-1*. We found that, with conjugation rates free to vary in *dao1-1*, a wide range of parameter sets can fit the quantitative data. (Fig. 2C). Running the parameter fitting algorithm a number of times, we generated 100 different parameter sets which all result in good agreement of the model with data (well within the bounds of statistical experimental error). Plotting the distribution of each of the fitted parameter values shows that there is a limited degree of variability in some parameters between parameter sets (Fig. 2C). Fig. 2D shows that the predicted relative changes between w.t. and *dao1-1* match those observed for the six key metabolites. Fig. 2E and F show that the rates of conjugation via GH3 increase more than 400-fold (to IAA-Asp) and more than 200-fold (to IAA-Glu) in *dao1-1* compared to w.t., consistently across parameter sets.

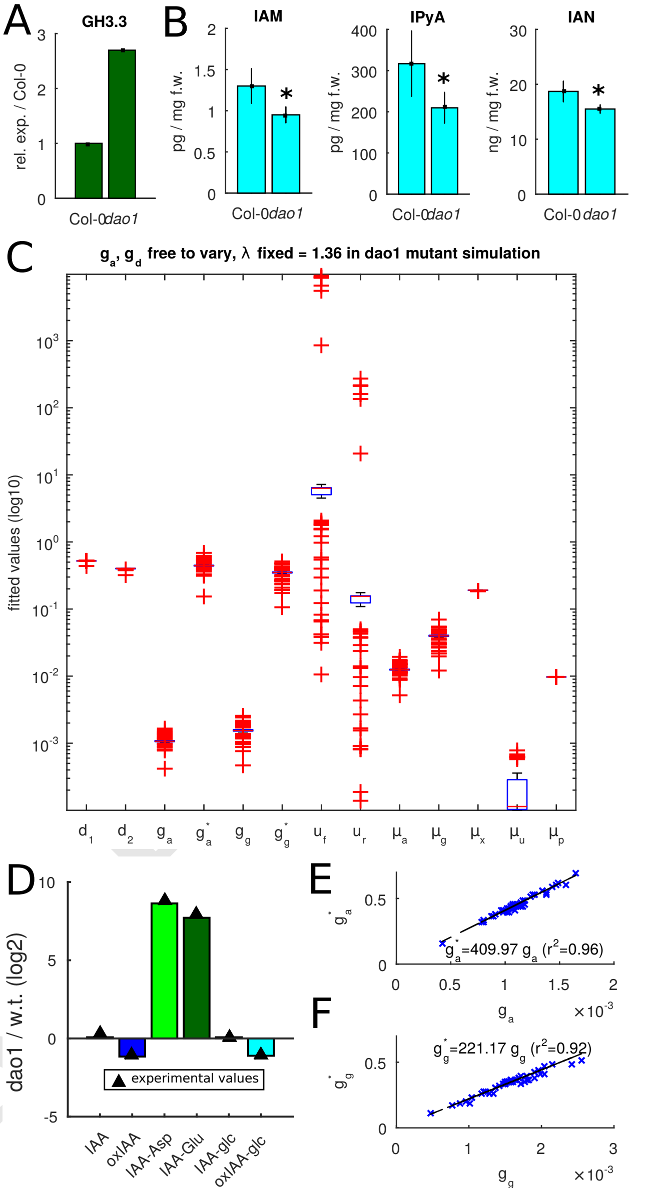

Fig. 2. Experimental evidence and model optimisation support the hypothesis that, in addition to reduced oxidation, both IAA biosynthesis and conjugation are increased in *dao1-1*. (**A**) Expression of the conjugating enzyme *GH3.3* is elevated in *dao1-1*. (**B**) Levels of the IAA precursors IAM, IPyA and IAN are all significantly reduced in dao1-1. Asterisks indicate statistically significant differences from Col-0 (P<0.05, Student's t-test). (**C**) Box plot showing the first and third quartile (bottom and top of blue boxes), median (red lines), lowest and highest data points within $1.5\times$ the interquartile range (black whiskers), plus outliers (red + symbols) of 100 fitted parameter sets. With IAA biosynthesis and conjugation rates free to vary in *dao1-1* a wide range of parameter sets can fit the quantitative data. (**D**) Representative fit between model and data, *dao1-1* relative to w.t. simulation. (**E,F**) Conjugation rates in *dao1-1* (g_a^* and g_g^*) are predicted to be more than 200-fold larger than in w.t. (g_a and g_g), consistently across 100 parameter sets.

Dynamic regulation of *AtDAO1* and *GH3* by auxin allows a context-dependent homeostatic response to changes in auxin. As expected for important components of the auxin homeostasis machinery, *AtDAO1* and *GH3* genes are auxin inducible [11, 16]. Affymetrix-based transcriptomic analysis of auxin treated root tips revealed that *GH3.3* mRNA is induced very rapidly (peaking at two hours) while *AtDAO1* mRNA is induced more slowly (peaking at the final, four hour time-point). RT-qPCR-based transcriptomic analysis also showed that *GH3.3* is up regulated 2.7-fold in *dao1-1* (Fig. 2A), and around 200-fold in wild type seedlings exposed to IAA (Fig. 3A, S1). In contrast, IAA-treated w.t. seedlings show at most a 75% increase in *AtDAO1* expression (Fig. 3A, S1). We conclude that *AtDAO1* and *GH3.3* are upregulated by auxin, over different timescales and concentration ranges and with different fold-changes in response.

To investigate the effect of these nonlinear feedbacks on auxin homeostasis we incorporate them into an extended model (Fig. 3B) in which the expression of both *AtDAO1* and *GH3* increase as the concentration of IAA increases. To model these nonlinearities we use Hill functions (Equations [2b]-[2c]), where the threshold parameters k_d and k_g determine the level of IAA at which gene expression reaches half-maximum, and the Hill coefficients n_d and n_g determine the sharpness of the transition from low to high expression. In the case of *AtDAO1* we see at most a doubling of the mRNA level from basal expression under IAA treatment, with no sharp switch in expression observed (Fig. 3A, S1), which suggests a half-maximum threshold similar to the basal IAA concentration. Hence, we fix $k_d = 1$ and the Hill coefficient $n_d = 1$, and fit the remaining model parameters to the steady state metabolic wild type and *dao1-1* data. The fitted nonlinear model shows good agreement with the data (Fig. S4) and demonstrates that a small increase in IAA biosynthesis rate (36%) can result in a much larger (> 100-fold) increase in the level of IAA-Asp and IAA-Glu conjugates.

Fig. 3C uses the estimated and fitted parameters to compare the contribution of the *GH3* and *AtDAO1* pathways to IAA degradation. While the contribution of *AtDAO1* increases slightly over the range shown and is still active even at low levels of IAA, conjugation rates are much lower at and below basal levels ($IAA \leq 1$) but rapidly increase as IAA increases, so that for high levels of IAA ($IAA \geq 2$) the conjugation pathway is dominant.

Fig. 3D-F shows the temporal response of the model after changing the $[IAA]$ input rate, λ, from the basal steady-state value ($\lambda = 1$). To compare the relative importance of the *AtDAO1* and *GH3* degradation pathways, as well as the 'full' model with both up-regulated by IAA, we also show three alternate versions, one where only *AtDAO1* is induced by auxin, one where only *GH3* is induced by auxin, and one where neither response is induced. With the full model there is a clearly a homeostatic response, with a transient peak, after which the steady-state level of IAA is much lower than the steady-state level without any $AtDAO1/GH3$ induction. For a large change in IAA input (Figure 3D) this homeostasis is much more rapid and pronounced than for a relatively small change in IAA input (Figure 3E). This difference in homeostatic responses is due to variations in the magnitude and speed of *AtDAO1* and *GH3* responses to increased IAA as can be inferred from the simulations where the inducibility of one or the other is switched off. In the absence of *GH3* induction, homeostasis is greatly reduced for a 10-fold increase in IAA input (Fig. 3D), while for a 2-fold reduction the homeostatic response is largely unchanged from the full model (Fig. 3F). Conversely, in the absence of *AtDAO1* regulation the homeostatic effect is only slightly reduced for a 10-fold IAA increase, while it is undetectable for a 2-fold-reduction in IAA input. For a 2-fold increase in IAA input both the AtDAO1 and GH3 pathways contribute to IAA homeostasis (Fig. 3E).

Mathematical modeling of these feedbacks on auxin degradation suggests *AtDAO1* is more effective for auxin homeostasis at lower auxin concentrations, while GH3s are much more important at high auxin levels. This is illustrated further in Figure 3G, which shows the IAA steady state for a range of values of the auxin input rate λ, for each of the model variants described above. Here, $IAA = 1$ corresponds to typical physiological levels. Around this level and below the *AtDAO1* degradation pathway is the more active, but above this level the *GH3* pathway becomes more active, and eventually is much more important than *AtDAO1* in removing large quantities of excess IAA.

Multicellular root modeling predicts auxin accumulation in epidermal tissues. We developed a spatial model for auxin transport and metabolism, combining our compartmental ODE model for IAA metabolism and IAA-dependent induction of *AtDAO1* and *GH3* (described above), with the multicellular model for IAA transport described in [17]. The multicellular model is based on actual root cell geometries and auxin influx and efflux carrier subcellular localizations. The IAA concentration is defined in each cell, together with terms for the rates of carrier-dependent transport between cells.

Following [17], we prescribed PIN, AUX and LAX carrier distributions in our virtual root tissues, with the PIN carriers polarised according to reports in the literature and our own observations using anti-PIN antibodies. The model also incorporated a weak background efflux to account for low levels of nonpolar PIN and for the presence of other transporters such as ABCB. We specified small auxin production rates within every cell and higher auxin production in the QC and columella initials. The model also captured auxin diffusion through the apoplast, as measured by [18]. We treated auxin concentrations as uniform within each cell, due to the small size of cells in this region and relatively rapid auxin diffusion within the cytoplasm compared to within the apoplast [18–20]. This is in contrast with the larger cells further from the root tip, where subcellular variations in auxin have previously been considered [21, 22].

The resulting model can be described by a system of ODEs for the auxin concentrations within each cell and each segment of apoplast. For details and model parameter values see *SI Appendix*, [17]. As done previously, we included a flux of auxin from the shoot by prescribing a non-zero auxin concentration within the stele cells at the boundary of the modeled tissue. In the epidermal, cortical, and endodermal cells we assume that the auxin concentrations have reached their far-field asymptotic values, hence setting them equal to those in neighbouring (rootward) cells of the same type. This implies an appropriate shootward flux of auxin through the outer tissue layers [19]. Starting from an initial condition in which all remaining concentrations equal zero, we simulated the ODEs until the concentrations and fluxes reached a steady state.

Embedding our homeostasis model into a multicellular context allows us to predict the effect of the *dao1-1* mutant on IAA levels and distribution in root tissues when compared to the wild type. Simulations using our combined transport and homeostasis model predict that the wild type IAA distribution (Fig. 4A) is in good agreement with spatial patterns inferred from the DII-VENUS fluorescent auxin signalling sensor [17]. Though the spatial pattern in the *dao1-1* mutant is similar to w.t., the total concentration of IAA was predicted to increase by 26%, consistent with the metabolite data (Fig. 1B). Very interestingly, the simulated increase in auxin is predicted to be spatially inhomogeneous, with auxin concentrations in outer root tissues increased $> 40\%$ (Fig. 4B). The predicted increase in IAA in the *dao1-1* mutant outer root tissues is consistent with the observed extra elongated root hair phenotype, which

DRAFT

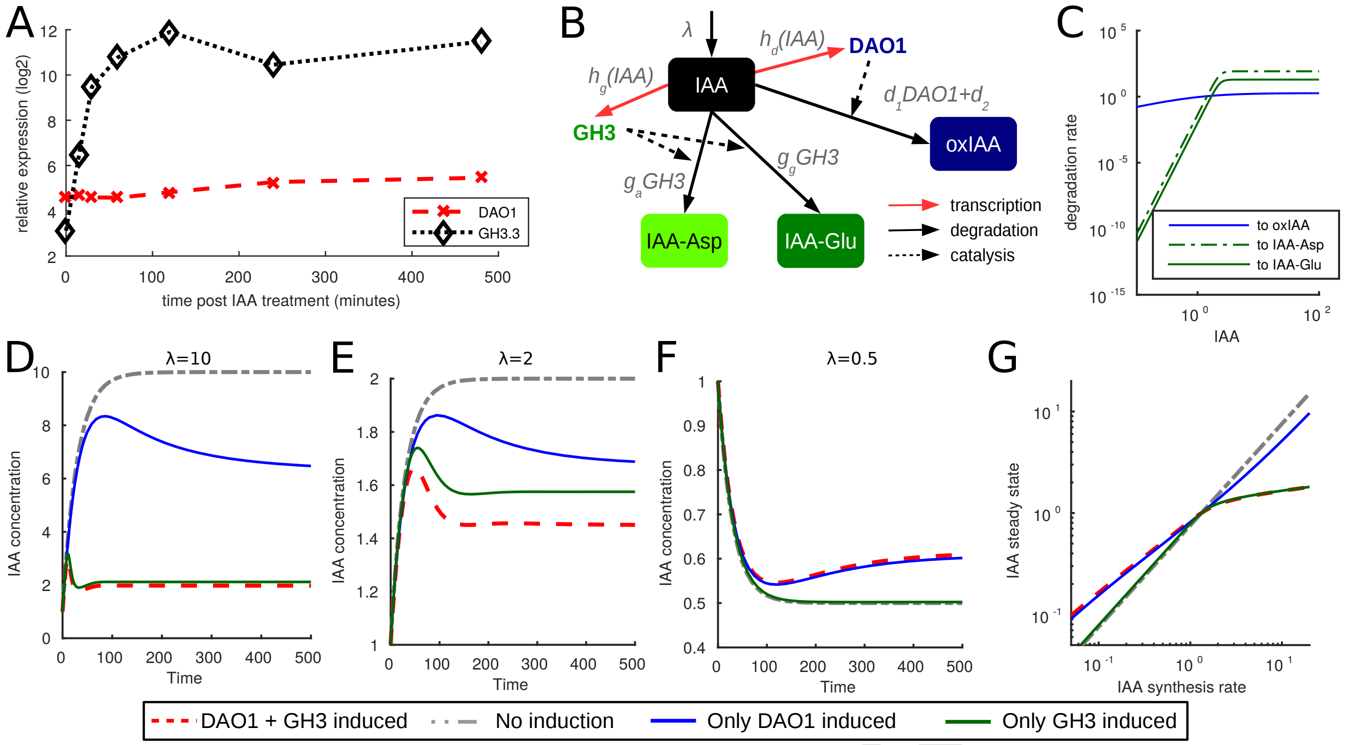

Fig. 3. *AtDAO1* transcriptional regulation by IAA provides sensitivity at low auxin concentrations, whilst *GH3* regulation contributes to homeostasis at high auxin concentrations. (**A**) Affymetrix data showing *AtDAO1* and *GH3.3* transcript abundance in micro-dissected root tips at time points after IAA treatment. (**B-G**) Mathematical modeling of these feedbacks on auxin degradation suggests *AtDAO1* is more effective in auxin homoeostasis at lower auxin concentrations, while *GH3*s contribute much more at high levels of auxin. (**B**) Submodel for IAA metabolism indicating the IAA-dependent transcription of *AtDAO1* and *GH3*. (**C**) Effective *AtDAO1* and *GH3* dependent IAA degradation rates at steady state for fixed levels of IAA input. (**D,E**) Temporal response to a 10- and 2-fold increase in IAA input with different combinations of modeled regulation. *GH3* regulation is dominant. In each case the model is shown with both *AtDAO1* and *GH3* inducible by auxin, only *AtDAO1* inducible, and only *GH3* inducible. (**F**) Temporal response to a 2-fold decrease in IAA input with different combinations of modeled regulation. *AtDAO1* regulation is dominant. (**G**) The steady-state patterns seen in (D)-(F) are found across a wide range of IAA input rates.

is known to be auxin dependent [23].

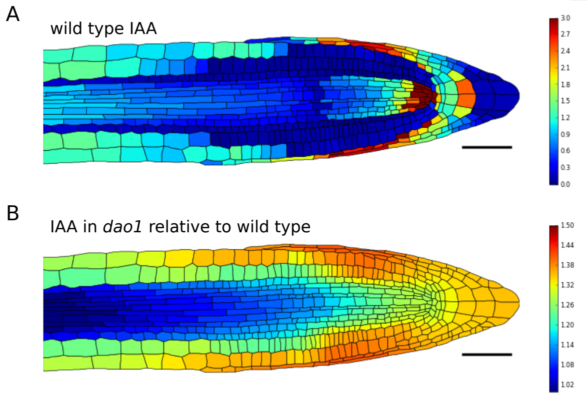

Fig. 4. Multicellular simulation, showing auxin accumulation in outer tissues of the root apex in *dao1-1* relative to wild type. (**A**) Predicted IAA in the wild type simulation, relative to the fixed reference value of IAA=1 in the stele at the shootward end of the tissue, as defined in the boundary conditions. (**B**) In *dao1-1*, auxin is up to 40% higher in the epidermis, which is consistent with increased RSL4 expression causing the increased root hair phenotype seen in the *dao1-1* mutant [11].

Discussion

Our systems-based study has revealed that auxin homeostasis is controlled by highly redundant regulatory mechanisms involving auxin oxidation, conjugation and synthesis pathways. These auxin homeostasis regulatory mechanisms are also highly non-linear, involving multiple feedback loops that control the expression of AtDAO1 IAA oxidase and GH3 IAA conjugation enzymes. These regulatory mechanisms also operate across a range of spatial and temporal scales and auxin concentrations. For example, *AtDAO1* and *GH3* exhibit contrasting slow and rapid temporal expression dynamics, respectively. These differences in timing of *AtDAO1* and *GH3* induction by auxin are likely to be functionally very important. The slow auxin induction of *AtDAO1* ensures that perturbations in this signal can still cause a desired developmental response, while helping the cell maintain an optimal level of auxin. *GH3* on the other hand is only induced when auxin is high and so may be expressed rapidly in order to remove excess auxin as quickly as possible. The triggering of the GH3 degradation pathway at high levels of auxin is possibly a stress response to excess auxin levels, and is likely in effect during many lab experiments when large amounts of exogenous auxin is applied. However, Kramer and Ackelsberg [24] recently suggested that the GH3 conjugation pathway may be important at sites of high auxin accumulation during normal growth such as lateral root primordia or within the shoot apical meristem.

Despite these myriad auxin homeostasis mechanisms operating in plants, our multicellular model predicted that disrupting just the IAA oxidase *AtDAO1* is still able to perturb auxin levels in selected root tissues. This included elevating auxin levels in the *dao1-1* mutant epidermis (Fig. 4B), the tissue from which root hairs originate and elongate in an auxin-dependent manner.

Datta et al. [25] have recently demonstrated that root hair length is directly proportional to the abundance of a bHLH transcription factor RSL4 whose expression is auxin inducible. Hence, we would predict (based on our multicellular model simulations) that RSL4 and root hair length would increase in proportion to the >40% increase in auxin levels in the *dao1-1* mutant epidermis. Consistent with our model predictions, Porco et al [11] report similar increases in *RSL4* mRNA abundance and root hair length in the *dao1-1* mutant epidermis experimentally. Hence, we reason that auxin levels may also be perturbed in other *dao1-1* mutant tissues and/or stages of development. This helps explain why, despite the highly redundant organisation of the auxin homeostasis, *dao1-1* exhibits a number of subtle auxin-related mutant phenotypes in root, shoot and floral tissues [11, 12].

Materials and Methods

$[G]$ representing GH3s. $[D]$ and $[G]$ are assumed to be produced

Plant material and growth conditions. *Arabidopsis thaliana* Columbia-0 (Col-0) was used as wild type in all experiments. All T-DNA insertion mutants were obtained from the NASC (Nottingham Arabidopsis Stock Centre). Wild type and mutant plants were grown as described in [11].

RNA isolation and analysis. Sterilized seeds were plated on half MS media and stratified at 4°C for 24h to synchronise germination then transferred to a controlled growth chamber. 7 day old seedlings on plates were then transferred to MS media containing 1uM IAA for varying lengths of time. RNA was extracted from root tips and used for microarray analysis with the Affymetrix ATH1 array.

IAA metabolite profiling. *Arabidopsis thaliana* wild type Col-0 and the *dao1-1* mutant were grown under LD conditions for 7 or 10 days. Whole seedlings or dissected tissues were collected in 5 replicates (20 mg tissue per sample). Sample purification and quantification of IAA metabolites was performed as described in [26].

Mathematical models and parameter estimation. Here we summarize our mathematical models of the auxin homeostasis network. For full details of all models, definitions of model variables and parameters, and parameter estimation, see *SI appendix*.

IAA metabolism model: The simplest model of the pathway shown in Figure 1A has a constant rate of IAA biosynthesis (λ), and linear rates of degradation and conversion from one form of auxin to another:

$$\frac{d[IAA]}{dt} = \lambda - (u_f + g_a + g_g + d_1 + d_2)[IAA] + u_r[IAA\text{-}glc] \quad [1a]$$

$$\frac{d[oxIAA]}{dt} = (d_1 + d_2)[IAA] - \mu_x[oxIAA] \quad [1b]$$

$$\frac{d[IAA\text{-}Asp]}{dt} = g_a[IAA] - \mu_a[IAA\text{-}Asp] \quad [1c]$$

$$\frac{d[IAA\text{-}Glu]}{dt} = g_g[IAA] - \mu_g[IAA\text{-}Glu] \quad [1d]$$

$$\frac{d[IAA\text{-}glc]}{dt} = u_f[IAA] - (u_r + \mu_u)[IAA\text{-}glc] \quad [1e]$$

$$\frac{d[oxIAAglc]}{dt} = \mu_x[oxIAA] + \mu_u[IAA\text{-}glc] - \mu_p[oxIAA\text{-}glc]. \quad [1f]$$

Inducible *AtDAO1-GH3* model: We extend Equations (1a)-(1f) by assuming that the rate of conversion of IAA to oxIAA (d_1) is proportional to the level of a new variable $[D]$ representing AtDAO1, and the rates of conjugation of IAA to IAA-Asp (g_a) and IAA-Glu (g_g) are proportional to the level of another new variable in response to $[IAA]$, represented by Hill functions, and to decay linearly, so that:

$$g_a = \hat{g}_a[G], \quad g_g = \hat{g}_g[G], \quad d_1 = \hat{d}_1[D], \quad [2a]$$

$$\frac{d[D]}{dt} = \eta_d\left(\frac{[IAA]^{n_d}}{k_d^{n_d} + [IAA]^{n_d}} - [D]\right), \quad [2b]$$

$$\frac{d[G]}{dt} = \eta_g\left(\frac{[IAA]^{n_g}}{k_g^{n_g} + [IAA]^{n_g}} - [G]\right). \quad [2c]$$

Multicellular model: see the *SI Appendix*.

ACKNOWLEDGMENTS. NM, LB, UV, TH, MW, JRK, MJB and MRO acknowledge the support of the Biological and Biotechnology Science Research Council (BBSRC) responsive mode and CISB awards to the Centre for Plant Integrative Biology. AR and MJB also acknowledge the support of the Saudi Arabian Ministry of Higher Education. NM, MJB and MRO acknowledge European Research Council Futureroots funding. LB acknowledges funding from the Leverhulme Trust.

1. Vanneste S, Friml J (2009) Auxin: A trigger for change in plant development. *Cell* 136(6):1005 – 1016.
2. Ludwig-Müller J (2011) Auxin conjugates: their role for plant development and in the evolution of land plants. *Journal of Experimental Botany*.
3. Staswick PE et al. (2005) Characterization of an arabidopsis enzyme family that conjugates amino acids to indole-3-acetic acid. *The Plant Cell* 17(2):616–627.
4. Östin A, Kowalyczk M, Bhalerao RP, Sandberg G (1998) Metabolism of indole-3-acetic acid in *Arabidopsis*. *Plant Physiology* 118(1):285–296.
5. Kai K, Horita J, Wakasa K, Miyagawa H (2007) Three oxidative metabolites of indole-3-acetic acid from *Arabidopsis thaliana*. *Phytochemistry* 68(12):1651–1663.
6. Pěnčík A et al. (2013) Regulation of auxin homeostasis and gradients in *Arabidopsis* roots through the formation of the indole-3-acetic acid catabolite 2-oxindole-3-acetic acid. *The Plant Cell* 25(10):3858–3870.
7. Jackson RG et al. (2001) Identification and biochemical characterization of an *Arabidopsis* indole-3-acetic acid glucosyltransferase. *Journal of Biological Chemistry* 276(6):4350–4356.
8. Peer WA, Cheng Y, Murphy AS (2013) Evidence of oxidative attenuation of auxin signalling. *Journal of Experimental Botany* 64(9):2629–2639.
9. Tanaka K et al. (2014) Ugt74d1 catalyzes the glucosylation of 2-oxindole-3-acetic acid in the auxin metabolic pathway in *Arabidopsis*. *Plant and Cell Physiology* 55(1):218–228.
10. Voß U et al. (2015) The circadian clock rephases during lateral root organ initiation in *Arabidopsis thaliana*. *Nat Commun* 6.
11. Porco S et al. (2016) The dioxygenase-encoding *AtDAO1* gene controls iaa degradation and homeostasis in *Arabidopsis*. *Proc Natl Acad Sci USA* (co-submitted manuscript).
12. Zhang J (2016) Oxidative inactivation by DAO1 regulates growth in *Arabidopsis thaliana*. *Proc Natl Acad Sci USA* (co-submitted manuscript).
13. Butler ED, Gallagher TF (2000) Characterization of auxin-induced arro-1 expression in the primary root of *Malus domestica*. *J Exp Bot* 51(351):1765–1766.
14. Zhao Z et al. (2013) A role for a dioxygenase in auxin metabolism and reproductive development in rice. *Developmental Cell* 27(1):113–122.
15. Thomas SG, Phillips AL, Hedden P (1999) Molecular cloning and functional expression of gibberellin 2-oxidases, multifunctional enzymes involved in gibberellin deactivation. *Proc Natl Acad Sci USA* 96(8):4698–4703.
16. Park JE et al. (2007) GH3-mediated auxin homeostasis links growth regulation with stress adaptation response in arabidopsis. *J Biol Chem* 282(13):10036–10046.
17. Band LR et al. (2014) Systems analysis of auxin transport in the *Arabidopsis* root apex. *The Plant Cell* 26(3):862–875.
18. Kramer EM, Frazer NL, Baskin TI (2007) Measurement of diffusion within the cell wall in living roots of *Arabidopsis thaliana*. *J Exp Bot* 58(11):3005–3015.
19. Band LR, King JR (2012) Multiscale modelling of auxin transport in the plant-root elongation zone. *J Math Biol* 65(4):743–785.
20. Swarup R et al. (2005) Root gravitropism requires lateral root cap and epidermal cells for transport and response to a mobile auxin signal. *Nat Cell Biol* 7(11):1057–1065.
21. Laskowski M et al. (2008) Root system architecture from coupling cell shape to auxin transport. *PLoS Biol* 6(12):e307.
22. Payne RJH, Grierson CS (2009) A theoretical model for ROP localisation by auxin in *Arabidopsis* root hair cells. *PLoS One* 4(12):e8337.
23. Pitts RJ, Cernac A, Estelle M (1998) Auxin and ethylene promote root hair elongation in *Arabidopsis*. *The Plant Journal* 16(5):553–560.
24. Kramer EM, Ackelsberg EM (2015) Auxin metabolism rates and implications for plant development. *Frontiers in Plant Science* 6:150.
25. Datta S, Prescott H, Dolan L (2015) Intensity of a pulse of RSL4 transcription factor synthesis determines *Arabidopsis* root hair cell size. *Nature Plants* 1(15138).
26. Novák O et al. (2012) Tissue-specific profiling of the *Arabidopsis thaliana* auxin metabolome. *The Plant Journal* 72(3):523–536.
27. Ljung K (2013) Auxin metabolism and homeostasis during plant development. *Development* 140:943–950.
28. Pradal C, Dufour-Kowalski S, Boudon F, Fournier C, Godin C (2008) OpenAlea: a visual programming and component-based software platform for plant modelling. *Funct Plant Biol* 35(10):751–760.

DRAFT

SUPPLEMENTAL INFORMATION:
Dynamic Regulation of *AtDAO1* and *GH3* modulates auxin homeostasis

1 Linear ODE model of IAA degradation

To investigate whether the conceptual model of the main IAA degradation pathways summarised in Fig. 1A (main text) is consistent with the metabolite data given in Fig. 1B (main text) a simple linear ordinary differential equation model was formulated, as described below in Sections 1.1 and 1.2. The model simulates the biosynthesis of IAA and its subsequent conversion to IAA-glc via UGT, to IAA-Asp and IAA-Glu via *GH3*, and to oxIAA via *AtDAO1/2*. IAA-glc and oxIAA can both be conjugated further to form oxIAA-glc, and this, along with the conjugates IAA-Asp and IAA-Glu, are then degraded at fixed rates (to prevent accumulation of these products in the model system).

1.1 Model reactions

In the following the empty set notation is used to denote a fixed pool of molecules from and into which model variables can be respectively synthesised and degraded. We assume all substrates such the amino acids Asp and Glu are available in excess so that this pool is neither depleted or increased. For a review of the IAA metabolic pathways modelled here see [27].

We initially consider the input of IAA to the system to be at some fixed rate λ:

$$\emptyset \xrightarrow{\lambda} \text{IAA}.$$

This IAA synthesis step is considered in more detail, taking into account quantitative IAA precursor data, in Section 2.

The oxidative pathway is modelled by the conversion of IAA to oxIAA by the combined action of *AtDAO1* and *AtDAO2* with respective rate constants d_1 and d_2, the subsequent conversion of oxIAA to oxIAA-glc with rate μ_x, and finally the degradation of oxIAA-glc with rate μ_p:

$$\text{IAA} \xrightarrow{d_1 + d_2} \text{oxIAA} \xrightarrow{\mu_x} \text{oxIAA-glc} \xrightarrow{\mu_p} \emptyset.$$

GH3 mediated conjugation is modelled by two pathways, one which models the conjugation of IAA with Aspartic acid with rate g_a to produce IAA-Asp, and another which models the conjugation of IAA with Glutamate with rate g_g to produce IAA-Glu:

$$\text{IAA} \xrightarrow{g_a} \text{IAA-Asp} \xrightarrow{\mu_a} \emptyset, \quad \text{IAA} \xrightarrow{g_g} \text{IAA-Glu} \xrightarrow{\mu_g} \emptyset,$$

where μ_a and μ_g are the respective degradation rates of IAA-Asp and IAA-Glu.

Finally the conversion of IAA to IAA-glc via UGT is modelled with rate constant u_f, with the reverse reaction also included with rate u_r. IAA-glc can also be converted to oxIAA-glc with rate μ_u, which as previously stated degrades with rate μ_p:

$$\text{IAA} \underset{u_r}{\overset{u_f}{\rightleftharpoons}} \text{IAA-glc} \xrightarrow{\mu_u} \text{oxIAA-glc} \xrightarrow{\mu_p} \emptyset.$$

1.2 Model equations

Using the law of mass action, we cast the set of the reactions described in Section 1.1 as a set of ordinary differential equations for six variables:

$$\frac{d[IAA]}{dt} = \lambda - (u_f + g_a + g_g + d_1 + d_2)[IAA] + u_r[IAA\text{-}glc] \tag{1a}$$

$$\frac{d[oxIAA]}{dt} = (d_1 + d_2)[IAA] - \mu_x[oxIAA] \tag{1b}$$

$$\frac{d[IAA\text{-}Asp]}{dt} = g_a[IAA] - \mu_a[IAA\text{-}Asp] \tag{1c}$$

$$\frac{d[IAA\text{-}Glu]}{dt} = g_g[IAA] - \mu_g[IAA\text{-}Glu] \tag{1d}$$

$$\frac{d[IAA\text{-}glc]}{dt} = u_f[IAA] - \mu_u[IAA\text{-}glc] - u_r[IAA\text{-}glc] \tag{1e}$$

$$\frac{d[oxIAA\text{-}glc]}{dt} = \mu_x[oxIAA] + \mu_u[IAA\text{-}glc] - \mu_p[oxIAA\text{-}glc] \tag{1f}$$

Time is dimensionless, scaled by the dimensional biosynthesis rate (λ_w), divided by the IAA concentration in wild type ($[IAA]_w$), so that for wild type $\lambda = 1$. All other model species are nondimensionalised by scaling with $[IAA]_w$.

1.3 *dao1-1* mutant simulations

We use the * superscript notation to indicate the mutant value when parameter values may differ from their wild type values in the *dao1-1* simulations. For example the wild type rate of *AtDAO1* mediated oxidation is denoted d_1, while the value in the *dao1-1* mutant is denoted d_1^*.

The simplest way to model the *dao1-1* knock-out mutant is to set $d_1^* = 0$ in Equation (1). However, if this is the only difference between the wild type and mutant simulations, it is not possible to get good agreement between the model steady states and the metabolic data (Figs. 1C, S2) when running the parameter fitting algorithm (see Section 3). The best-fit parameter set is given in Table S1 and used as the base parameter set for further modifications of parameter values in the *dao1-1* simulations (Figure 1D-E, main text).

Based on this fitting of the initial model, and with support from further experimental data (Figure 2A,B, main text) in subsequent parameter fitting exercises we may also allow the IAA synthesis rate (λ^*) and the conjugation rates (g_a^* and g_g^*) to vary from their wild type values in the *dao1-1* mutant simulations. Figure 1D, main text uses the parameters in Table S1, except $g_a^* = 10g_a$ and $g_g^* = 10g_g$, while in Figure 1E $g_a^* = 10g_a$, $g_g^* = 10g_g$ and $\lambda^* = 10\lambda$.

2 IAA precursors

To fix the IAA synthesis rate in *dao1-1* (λ^*), we assume that IAA precursors have constant production rates (which do not vary between w.t. and *dao1-1*), and that each precursor is converted to IAA at a rate that is different in *dao1-1* compared to wild type.

If we denote the pool of IAA precursors $[IAA_p]_w$ in w.t. and $[IAA_p]_m$ in *dao1-1* and assume they are governed by the following:

$$\frac{d[IAA_p]_w}{dt} = \delta - \lambda[IAA_p]_w,$$

$$\frac{d[IAA_p]_m}{dt} = \delta - \lambda^*[IAA_p]_m,$$

where δ is the constant synthesis rate and λ and λ^* are the respective conversion rates to $[IAA]$, then at steady state we can rearrange to obtain:

$$\frac{\lambda^*}{\lambda} = \frac{[IAA_p]_m}{[IAA_p]_w}.$$

It follows that λ^* is inversely proportional to the corresponding drop in auxin precursor concentrations (0.74 averaged across IAM, IPyA and IAN from the whole-seedling metabolite data shown in Fig. 1 of the main text), giving $\lambda^* = 1.36$ (since $\lambda = 1$).

3 Parameter fitting

During the parameter fitting and all other single compartment simulations the systems of ODEs were solved from zero initial conditions in Matlab using the function **ode15s**. To simulate wild type plants the model(s) were run with one parameter set to steady state, and the same model was run with another parameter set to represent the *dao1-1* mutant. The steady state values were then compared with the data.

For the parameter estimation problems described below, we used the genetic algorithm (function **ga**) followed by local minimum search (function **fmincon**) from the Matlab Optimisation toolbox to minimize the error between the data and model simulations. The objective function to be minimised was:

$$f = \sum_{i \in X} \left(\frac{M_i^{wt} - D_i^{wt}}{\sigma_i^{wt}} \right)^2 + \sum_{i \in X} \left(\frac{M_i^{dao1} - D_i^{dao1}}{\sigma_i^{dao1}} \right)^2 \tag{2}$$

where M represents model steady state values, and D data points with associated error σ. The superscript wt denotes the wild type (Col-0), while dao1 denotes the dao1-1 knock out model variant and mutant plants. X is the set of metabolites IAA, $oxIAA$, IAA-Asp, IAA-Glu, IAA-glc and $oxIAA$-glc, the data for which is normalised relative to the wild type IAA measurement, consistent with the non-dimensional models. Unless stated all parameters were identical in the wild type and *dao1-1* simulations, save the mutant value for the *AtDAO1* oxidation rate $d_1^* = 0$, and constrained between 10^{-4} and 10^4. In all cases the wild type IAA production rate (λ) was fixed = 1.

The results of the parameter fitting in the simplest case, where only $d_1^* = 0$ differs from wild type in the *dao1-1* simulation, are shown in Fig. 1 (main text) and Fig. S2, and the parameters given in Table S1 (Set 1).

In Fig. 2 (main text) the linear model (Equations (1a)–(1f)) was fitted against the data, with g_a^* and g_g^* free to vary within the default constraints while λ^* was fixed $= 1.36$ (Section 2). The representative parameter set used to produce Fig. 2D and Fig. S3 is given in Table S1 (Set 2).

4 Inducible *AtDAO/GH3* model

4.1 Model formulation

The model is as the initial model (Equations (1a)-(1f)) except that the rate of conversion of IAA to oxIAA is proportional to the level of a new variable $[D]$ representing the level of *AtDAO1*, and the rates of conjugation of IAA to IAA-Asp and IAA-Glu are proportional to the level of another new variable $[G]$ representing the level of *GH3*, so that:

$$g_a = \hat{g}_a[G] \tag{3a}$$

$$g_g = \hat{g}_g[G] \tag{3b}$$

$$d_1 = \hat{d}_1[D] \tag{3c}$$

where $\hat{g}_a$, $\hat{g}_g$ and $\hat{d}_1$ are new parameters.

$[D]$ and $[G]$ are themselves produced at rates nonlinearly dependent on the level of $[IAA]$, represented by Hill functions, so that:

$$\frac{d[D]}{dt} = \eta_d \left(\frac{[IAA]^{n_d}}{k_d^{n_d} + [IAA]^{n_d}} - [D] \right), \tag{3d}$$

$$\frac{d[G]}{dt} = \eta_g \left(\frac{[IAA]^{n_g}}{k_g^{n_g} + [IAA]^{n_g}} - [G] \right). \tag{3e}$$

4.2 Parameter fitting

The inducible model was also fitted to the same metabolic data, using the same algorithm as the linear model (Section 3). The only parameter which differed from w.t. in *dao1-1* was λ^*, which was again fixed $= 1.36$. n_g and k_g were found using the parameter fitting but constrained $1 \leq n_g \leq 9$ and $10^{-4} \leq k_g \leq 10$. This upper bound on k_g was selected to ensure the response of *GH3* occurs within approximate physiological bounds of the level of IAA. The parameters n_d, k_d, η_d and η_g do not directly affect the fit with the metabolic data and were instead separately estimated based on the available *GH3* and *AtDAO1* mRNA expression data and fixed during the parameter fitting algorithm. We fit the remaining model parameters to the steady state metabolic wild type and *dao1-1* data. Since we see at most a doubling of the mRNA level from basal expression under IAA treatment, with no sharp switch in expression observed (Fig. S1A), we fix both the Hill coefficient (n_d) and the binding threshold $(k_d) = 1$. η_d and η_g affect the respective timescales over which *AtDAO1* and *GH3* can change. We estimate that gene expression will evolve over a slower timescale than biosynthesis, with *AtDAO1* changing more slowly than *GH3* so we set $\eta_d = 0.005$ and $\eta_g = 0.01$.

The representative fitted parameter set used to produce Fig. 3D-H main text and Figs. S4, S5 is given in Table S1 (Set 3), and is used as the basis for parameterisation of the multi-cellular model.

4.3 Model variants

For each of the model variants described below the model was run to steady state (using the parameters in Table S1) with $\lambda = 1$, then using these results as the initial conditions for a new set of simulations for $\lambda \in \{0.5, 2.0, 10.0\}$, the time-courses shown in Fig. 3E-G (main text) were plotted. The steady state of each model variant is also plotted for $0.05 \leq \lambda \leq 20$ in Fig. 3H (main text).

4.3.1 Only *AtDAO1* induced

The induction of *GH3* is switched off by setting:

$$\frac{d[G]}{dt} = 0,$$

with the initial condition that $[G]$ is equal to its steady state value in Equation (3e) when $[IAA] = 1$, i.e.:

$$[G] = \frac{1^{n_g}}{k_g^{n_g} + 1^{n_g}}.$$

4.3.2 Only *GH3* induced

Similarly, we switch off the induction of *AtDAO1* by setting:

$$\frac{d[D]}{dt} = 0, \quad [D] = \frac{1^{n_d}}{k_d^{n_d} + 1^{n_d}}.$$

4.3.3 No induction

Both inducible pathways are switched off by setting:

$$\frac{d[D]}{dt} = 0, \quad [D] = \frac{1^{n_d}}{k_d^{n_d} + 1^{n_d}}, \quad \frac{d[G]}{dt} = 0, \quad [G] = \frac{1^{n_g}}{k_g^{n_g} + 1^{n_g}}.$$

5 Multicellular model

The multicellular model is based on that of [17], in which auxin transport is embedded in a realistic root cell geometry, using a vertex-based data structure from the OpenAlea modeling framework [28], with experimentally observed locations for the PIN, AUX and LAX auxin efflux and influx carriers. To incorporate the *AtDAO1/GH3* homeostasis model we replace the linear production and degradation of IAA in [17] with the production and non-linear degradation defined in Equations (1a) & (3a)-(3c), so that in general terms for every cell i:

$$\frac{d[IAA]_i}{dt} = \alpha \text{ metabolism}_i + \text{transport}_i, \tag{4}$$

where $\alpha = 0.001$ (as in [17]) is a constant of proportionality to ensure that the relative contribution of metabolism and transport remains similar in the two models. All remaining model variables are simulated in every cell as in the inducible model.

The metabolism terms are identical to the right hand side of Equation (1a), with the IAA inducible versions of g_a, g_g and d_1 as defined in Equations (3a)-(3e). Parameter values are as estimated by the fitting algorithm as defined in Table S1, with two exceptions. To maximise the number of cells in which the IAA homeostasis model works at basal levels of IAA in the same way as described in the single compartment models (i.e. relatively low *GH3* conjugation, and intermediate levels of *AtDAO1* oxidation), we set the thresholds in the Hill functions for $[G]$ and $[D]$ 5× higher so that $k_d = 5.0$ and $k_g = 11.6135$. $\lambda = 1$ (wild-type) and $\lambda^* = 1.36$ (*dao1-1* mutant) in all cells except in the quiescent centre and columella initials, where $\lambda = 10$ and $\lambda^* = 13.6$, again reflecting the cell-type specific differences modelled in [17].

The transport terms, parameter values, initial conditions and efflux/influx carrier positions are identical to those defined in [17]. In summary, movement of IAA (denoted $[Auxin]$ in [17]) is simulated between every cell and its neighbouring apoplastic compartments, and between every apoplastic compartment and neighbouring apoplastic compartments (via quasi-steady state concentrations of IAA at the vertices between apoplastic compartments) using the following model:

$$\frac{d[IAA]_i}{dt} = \alpha \text{ metabolism}_i + \frac{1}{A_i} \sum_{j \in C_i} \sum_{k=1}^{N_{ij}} S_{ijk} J_{ijk}, \tag{5a}$$

$$\frac{d[IAA_a]_{ijk}}{dt} = \frac{1}{\delta}(J_{ijk} + J_{jik}) + \frac{1}{S_{ijk}} \sum_{m \in V_{ijk}} J_{ijkl}, \tag{5b}$$

where $[IAA]_i$ and A_i respectively denote the IAA concentration and area of cell i, and $[IAA_a]_{ijk}$ and S_{ijk} are, respectively, the IAA concentration and segment length of the k^{th} apoplastic compartment between cells i and j.

C_i is the set of neighbouring cells to cell i, N_{ij} is the number of apoplastic compartments between cells i and j, and V_{ijk} is the pair of vertices adjacent to apoplastic compartment ijk. δ is a parameter defining the apoplast width.

Finally, J_{ijk} is the flux from apoplast compartment ijk into cell i and J_{ijkl} is the flux into apoplastic compartment ijk from one of two neighbouring vertices $l \in V_{ijk}$. Both J_{ijk} and J_{ijkl} are defined as in [17].

For the boundary conditions, as done previously we included a flux of auxin from the shoot by prescribing a non-zero auxin concentration within the stele cells at the shootward boundary of the modeled tissue [17]. In the epidermal, cortical, and endodermal cells we assume that the auxin concentrations have reached their far-field asymptotic values, hence setting them equal to those in neighbouring (rootward) cells of the same type. This boundary condition is slightly different to that in [17], which sets the boundary cells to have zero auxin concentration, and implies an appropriate shootward flux of auxin through the outer tissue layers [19] — moreover, we have checked that this modification makes no significant difference to the model predictions.

Supplementary Figure Legends

Figure S1: qRT-PCR IAA dose response data showing *AtDAO1* and *GH3.3* mRNA expression levels increasing with IAA. 7 day old seedlings were treated with the stated IAA concentrations for 4 hours.

Figure S2: Best fit between simple *dao1-1* knock-out model and metabolic data, using Equations (1a)–(1f) and parameter values from Table S1 (Set 1).

Figure S3: Representative fit between *dao1-1* simulation (with $d_1^* = 0$, $\lambda^* = 1.36$, and g_a^* and g_g^* free to vary) and metabolic data, using Equations (1a)–(1f) and parameter values from Table S1 (Set 2).

Figure S4: Representative fit between model with inducible *AtDAO1* and *GH3* and metabolic data, showing absolute concentrations of auxin and its metabolites, using Equations (3a)–(3e) and parameter values from Table S1 (Set 3).

Figure S5: Representative fit between model with inducible *AtDAO1* and *GH3* and metabolic data, showing auxin and metabolite concentrations in *dao1-1* relative to wild type, using Equations (3a)–(3e) and parameter values from Table S1 (Set 3).

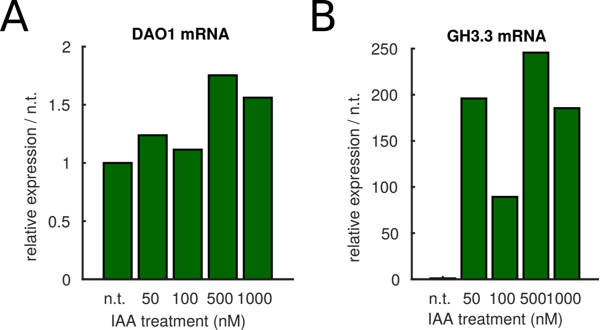
A
DAO1 mRNA
relative expression / n.t.
2
1.5
1
0.5
0
n.t.
50
100
500
1000
IAA treatment (nM)
B
GH3.3 mRNA
relative expression / n.t.
250
200
150
100
50
0
n.t.
50
100
5001000
IAA treatment (nM)

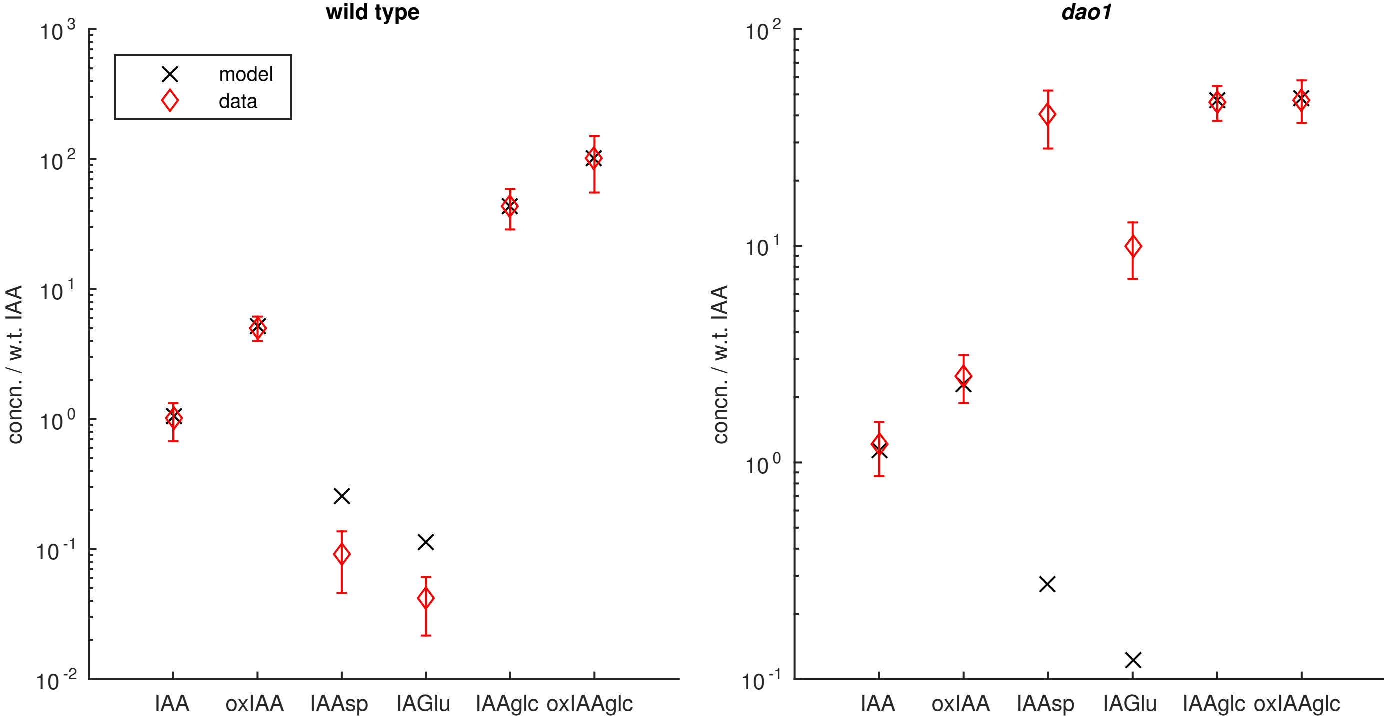
wild type
dao1
model
data
concn. / w.t. IAA
10^3
10^2
10^1
10^0
10^-1
10^-2
IAA
oxIAA
IAAsp
IAGlu
IAAglc
oxIAAglc

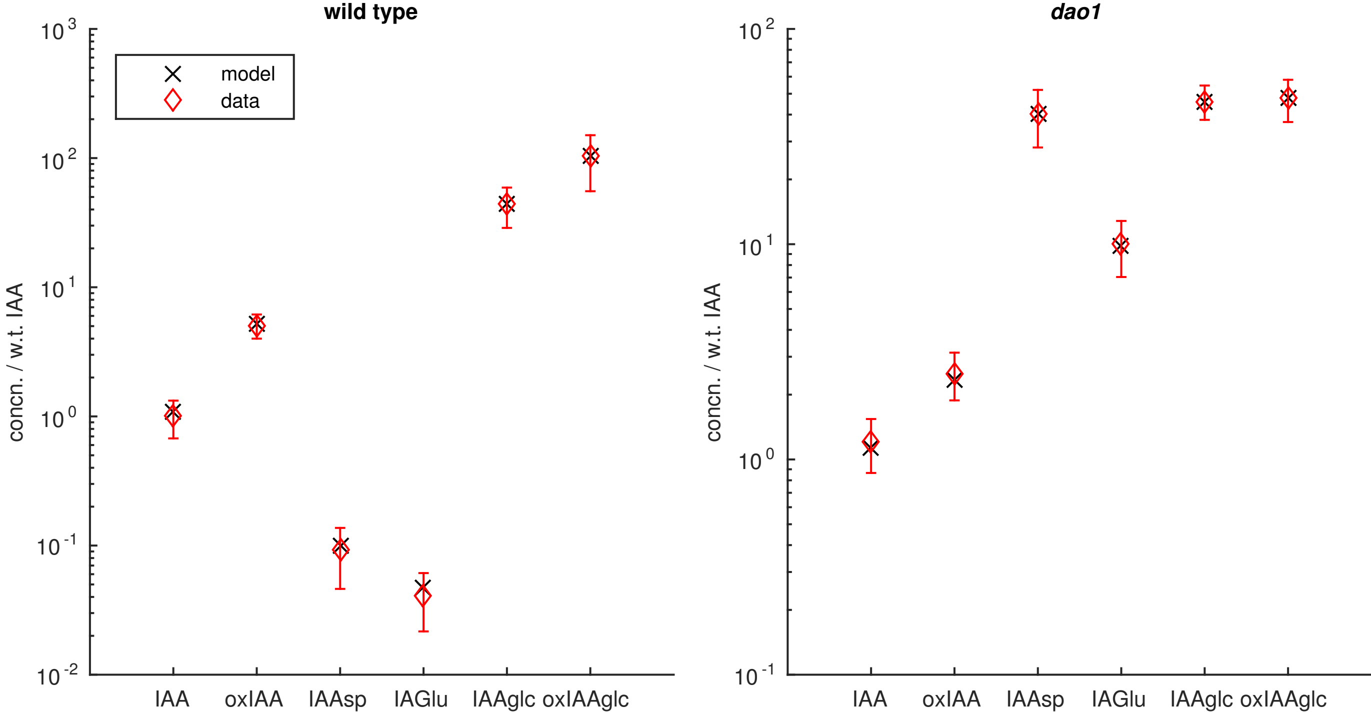
wild type
dao1
model
data
concn. / w.t. IAA
10^3
10^2
10^1
10^0
10^-1
10^-2
IAA
oxIAA
IAAsp
IAGlu
IAAglc
oxIAAglc

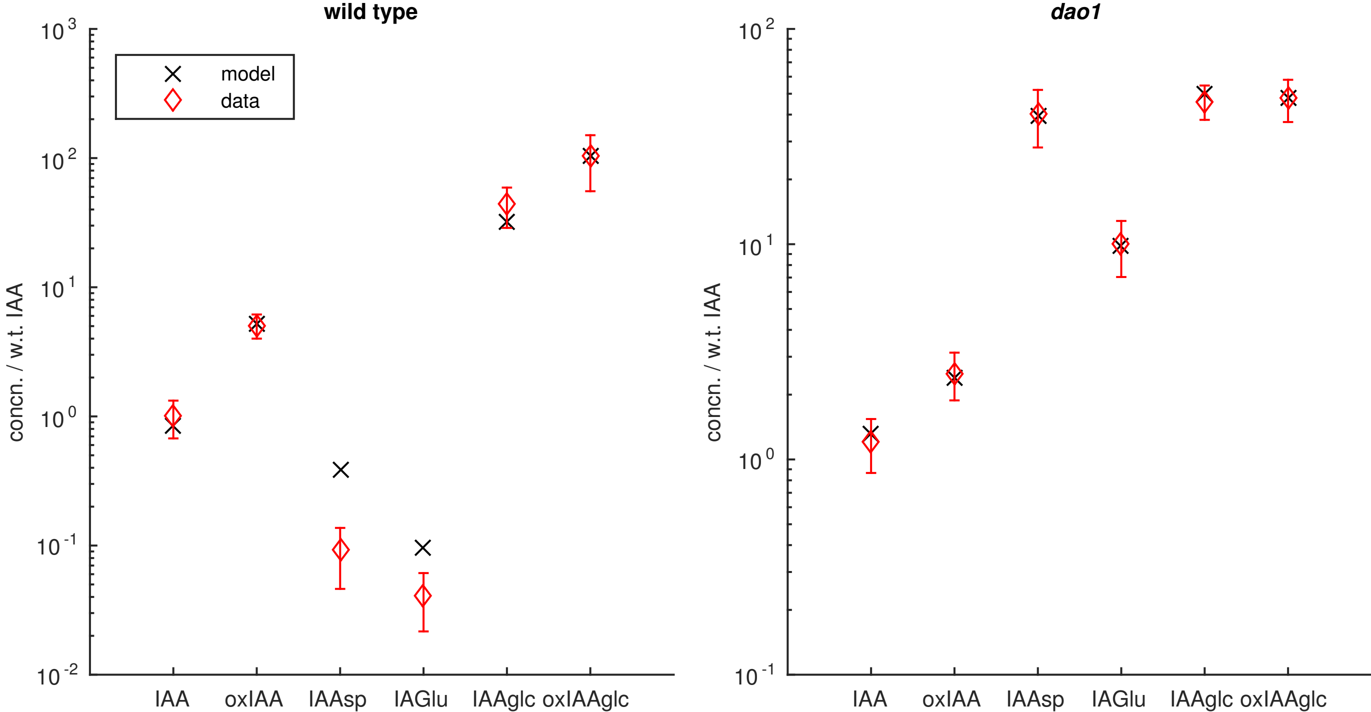
wild type
dao1
model
data
concn. / w.t. IAA
10^3
10^2
10^1
10^0
10^-1
10^-2
IAA
oxIAA
IAAsp
IAGlu
IAAglc
oxIAAglc
concn. / w.t. IAA
10^2
10^1
10^0
10^-1
IAA
oxIAA
IAAsp
IAGlu
IAAglc
oxIAAglc

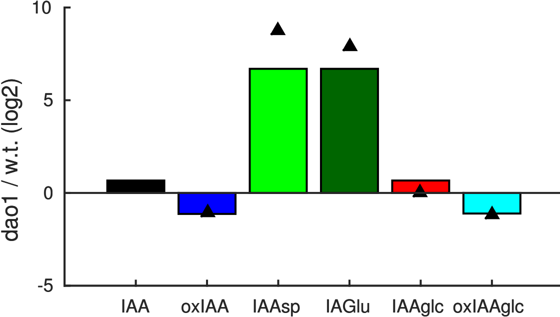

10
5
0
-5
dao1 / w.t. (log2)
IAA
oxIAA
IAAsp
IAGlu
IAAglc
oxIAAglc

Supplementary Table Legend

Table S1: Representative fitted parameter sets for the various models for auxin homeostasis. **Set 1:** simple *AtDAO1* knockout model ($d_1^* = 0$ in *dao1-1* simulation), using Equations (1a)–(1f). Parameters with superscript $*$ are for the *dao1-1* case. Here we assume $g_a = g_a^*$, $g_g = g_g^*$, $\lambda = \lambda^*$. **Set 2:** fitted parameter set, using Equations (1a)–(1f), for *dao1-1* simulation with $d_1^* = 0$, $\lambda^* = 1.36$, and g_a^* and g_g^* free to vary within the default constraints. **Set 3:** Representative fitted parameter set for model with inducible *AtDAO1* and *GH3*, used to produce Fig 3. (main text) and as the basis for the parameterisation of the multi-cellular model. See SI text for parameter constraints.

SUPPLEMENTARY TABLE 1:
Dynamic Regulation of *AtDAO1* and *GH3* modulates auxin homeostasis

Parameter	Set 1: *dao1-1* only differs in rate of IAA oxidation	Set 2: *dao1-1* differs in rates of IAA oxidation, biosynthesis and conjugation	Set 3: *dao1-1* only differs in rate of IAA oxidation, but *AtDAO1* and *GH3* are auxin inducible
λ	1	1	1
λ^*	1	1.36	1.36
d_1	0.0155	0.5224	1.8471
d_1^*	0	0	0
g_a	0.3324	0.0012	83.5023
g_a^*	0.3324	0.4382	83.5023
g_g	0.6399	0.0018	19.5837
g_g^*	0.6399	0.3594	19.5837
u_f	0.131	1.7864	515.7453
u_r	0.0042	0.0428	13.5992
μ_a	1.4581	0.0123	0.0185
μ_g	3.0129	0.0407	0.0174
μ_u	0.0001	0.0006	0.0002
d_2	0.0159	0.3856	0.3379
μ_p	0.0563	0.0012	0.0097
μ_x	0.0059	0.1860	0.1893
n_d	-	-	1
k_d	-	-	1
η_d	-	-	0.005
n_g	-	-	9.0
k_g	-	-	2.3227
η_g	-	-	0.01